CEAS Space J (2014) 6:79–98
DOI 10.1007/s12567-014-0060-2

ORIGINAL PAPER

Radiative heat transfer analysis in modern rocket combustion chambers

Florian Goebel · Björn Kniesner · Manuel Frey · Oliver Knab · Christian Mundt

Received: 17 October 2013 / Revised: 7 January 2014 / Accepted: 9 January 2014 / Published online: 24 January 2014
© CEAS 2014

Abstract Radiative heat transfer is analyzed for subscale and fullscale rocket combustion chambers for H_2/O_2 and CH_4/O_2 combustion using the P1 radiation transport model in combination with various Weighted Sum of Gray Gases Models (WSGGMs). The influence of different wall emissivities, as well as the results using different WSGGMs, the size of the combustion chamber and the coupling of radiation and fluid dynamics, is investigated. Using rather simple WSGGMs for homogeneous systems yields similar results as using sophisticated models. With models for nonhomogeneous systems the radiative wall heat flux (RWHF) decreases by 25–30 % for H_2/O_2 combustion and by almost 50 % for CH_4/O_2 combustion. Enlarging the volume of the combustion chamber increases the RWHF. The influence of radiation on the flow field is found to be negligible. The local ratio of RWHF to total wall heat flux shows a maximum of 9–10 % for H_2/O_2 and 8 % for CH_4/O_2 combustion. The integrated heat load ratio is around 3 % for H_2/O_2 and 2.5 % for CH_4/O_2 combustion. With WSGGMs for nonhomogeneous systems, the local ratio decreases to 5 % (H_2/O_2) and 3 % (CH_4/O_2) while the integrated ratio is only 2 % (H_2/O_2) and 1.3 % (CH_4/O_2).

This is an extended version of the paper published at the 5th European Conference for AeroSpace Sciences in 2013.

F. Goebel (✉) · C. Mundt
Institute of Thermodynamics, Universität der Bundeswehr München, LRT-10, 85577 Neubiberg, Germany
e-mail: florian.goebel@unibw.de

B. Kniesner · M. Frey · O. Knab
Airbus Defence and Space, System Analysis & Modeling TP22, 81663 Munich, Germany

Keywords Heat transfer · Radiative heat transfer · Gas radiation · CFD · Rocket combustion chamber

Abbreviations

CFD	Computational fluid dynamics
CWHF	Convective wall heat flux
NSMB	Navier–Stokes multiblock
RTE	Radiative transfer equation
RWHF	Radiative wall heat flux
SSME	Space shuttle main engine
TWHF	Total wall heat flux
WSGGM	Weighted Sum of Gray Gases Model

Latin symbols

a	Absorption coefficient
C	Absorption cross section
$\bar{C}$	Mean absorption cross section
f	Mixture fraction
e	Radiation energy
F	Blackbody distribution function
G	Incident radiation
h_q	Reduced enthalpy
h	Planck's constant
i	Radiation intensity
I	Number of gray gases
n	Refractive index
$\vec{n}$	Normal vector
N	Number density
q	Heat flux
r	Function of mixture
s	Direction
S	Path length
T	Temperature
w	Blackbody weight of gray gas

Greek symbols

Γ Goulard number
ε Emissivity
ϕ Scattering phase function
λ Wavelength
ρ Density
σ Scattering coefficient, Stefan–Boltzmann constant
ω Solid angle

Subscripts

b Blackbody property
c Carbon dioxide
i Index of gray gas, Numeration index
j Numeration index
mix Mixture
min Minimum
max Maximum
w Water vapor
λ Spectral value
∞ Freestream value

1 Introduction

Heat transfer analysis is crucial during the design process of rocket combustion chambers since the development of cooling systems and hence the life time of those chambers highly depends on the occurring heat loads. With their high gas temperatures above 3,000 K, rocket combustion chambers are likely influenced by radiative heat transfer that depends on temperature's fourth power.

The analysis of radiative heat transfer is a very complicated part of heat transfer calculations as it requires the solution of the radiative transfer equation (RTE) which depends on spatial, directional and spectral variables. Analytical solutions for the RTE have been achieved only for simplified cases whereas for most other applications numerical approximations are used to solve the RTE.

One of these numerical approximations is the P1 radiation model or method of spherical harmonics which simplifies the RTE by taking an angularly averaged intensity leading to a four-dimensional partial differential equation that depends only on spatial and spectral variables. The spectral dependencies can then be simplified using so-called spectral models from which one is the Weighted Sum of Gray Gases Model (WSGGM) that has been improved by several authors in the past [1–4]. Special WSGGM can also be applied to nonhomogeneous systems of nonuniform temperature, pressure and mole fractions [5].

The P1 radiation models and the WSGG models have been implemented into the CFD code NSMB [6] at the Institute of Thermodynamics of the Universität der Bundeswehr. Both models have been validated with simple cases for which analytical solutions of the RTE exist [7]. Within that work, the models have also been applied to the analysis of radiative heat transfer in the space shuttle main engine (SSME).

Together with former investigations by Naraghi et al. [8], Wang [9], Thellmann [10] and Goebel [7] the analysis concluded that for H_2/O_2 combustion integrated radiative heat loads to the wall have a share of nearly 8 % on the total heating of the wall whilst the local flux ratio exceeds 30 %. Assuming thrust identity for a fictitious CH_4/O_2 combustion in the space shuttle main engine 10 [10] and Goebel [11] have shown that radiation's integrated share on the total wall heat flux (TWHF) increases to nearly 9 %. More recently, nonhomogeneous WSGGM was also used in the simulation of radiative transfer in the SSME [12].

One of the shortcomings of all these former investigations is that the flow field of the SSME was predicted by CFD codes not taking into account the effects of propellant preparation on the heat load development especially in the injection region, which leads to an overestimation of the temperature field and hence the integral gas radiation contribution.

The aim of this work is therefore to assess radiative heat loads on the wall of various combustion chambers that are part of EADS Astrium's portfolio. As basis, flow field predictions by Astrium's in-house spray combustion CFD code Rocflam-II are used, which are validated against numerous experiments [13], taking into account propellant preparation effects such as propellant atomization, evaporation and mixing.

By using subscale and fullscale combustion chambers for H_2/O_2 and a subscale chamber for CH_4/O_2 combustion, the influence of a H_2O/CO_2 mixture on the radiative wall heat flux (RWHF) is investigated in comparison to single H_2O systems as well as the influence of the combustion chamber size on the RWHF and the influence of coupling radiation with fluid dynamics.

For these analyses, the P1 radiation model of NSMB in conjunction with the WSGG models mentioned above is employed. Results for the temperature, pressure and mole fractions of H_2O and CO_2 are imported from Rocflam-II into NSMB which calculates the parameters for the WSGGM and afterwards solves the P1 radiation transport equations. Detailed literature surveys are done to obtain reliable values for the emissivity of the combustion chamber wall.

The results in RWHF are compared to the convective wall heat flux (CWHF) for both H_2/O_2 and CH_4/O_2 combustion. The influence of wall emissivities and WSGG models is examined using the RWHF and its ratio to the TWHF, being the sum of RWHF and CWHF. The local ratio of RWHF to TWHF is investigated for both chambers and their corresponding propellant combination, yielding a qualitative overview of those regions in the combustion

chambers that are influenced most by the RWHF. The integrated ratio of RWHF to TWHF then gives the mean influence of radiation on the total heat loads. The influence of the combustion chamber's size on the RWHF is examined for H_2/O_2 combustion using various WSGGM. Coupling of radiation and flow is investigated by adding the divergence of radiative heat flux to the energy equation of Rocflam-II. In the end, the differences to the former investigations of the SSME are analyzed.

2 Numerical method

2.1 Theory of radiative transfer

The radiative transfer equation (RTE) in its spectral form is the basis of all radiative heat transfer investigations, [14, p. 562]

$$\frac{\mathrm{d}i_\lambda}{\mathrm{d}s} = \underbrace{a_\lambda \times i_{\lambda\mathrm{b}}(s)}_{\mathrm{A}} - \underbrace{(a_\lambda + \sigma_\lambda) \times i_\lambda(s)}_{\mathrm{B}} + \underbrace{\frac{\sigma_\lambda}{4\pi} \times \int_{4\pi} i_\lambda(s,\omega_i) \times \phi_\lambda(\omega_i,\omega) d\omega_i}_{\mathrm{C}}. \tag{1}$$

The RTE in Eq. (1) describes the change of a beam's intensity passing through a radioactively participating medium in the direction s. The change is due to a gain of intensity by emission and scattering (A and C) and a loss of intensity by absorption and scattering (B).

With the spectral intensity i_λ given as the solution of the RTE, the divergence of the spectral radiative heat flux can be calculated [14, p. 570]

$$\nabla q_{\mathrm{rad},\lambda} = a_\lambda \times (4 \times \pi \times i_{\lambda\mathrm{b}} - G_\lambda). \tag{2}$$

In Eq. (2), the spectral incident radiation G_λ is

$$G_\lambda = \int_{4\pi} i_\lambda \, d\omega. \tag{3}$$

and the spectral blackbody intensity $i_{\lambda\mathrm{b}}$ is given by Planck's law

$$i_{\lambda\mathrm{b}} = \frac{e_{\lambda\mathrm{b}}}{\pi} = \frac{2\mathrm{hc}_0^2}{n^2\lambda^5\left(e^{\mathrm{hc}_0/n\lambda\mathrm{kT}} - 1\right)}. \tag{4}$$

The divergence of the total radiative heat flux, necessary to couple the radiative heat transfer with the energy equation in CFD simulations, is obtained by integration over the entire spectrum

$$\nabla \vec{q}_{\mathrm{rad}} = \int_0^\infty \vec{\nabla} \vec{q}_{\mathrm{rad},\lambda} d\lambda. \tag{5}$$

The RTE in Eq. (1) is an integro-differential equation depending on 3 spatial, 2 directional and 1 spectral variable, which makes an analytical solution almost impossible for most engineering applications. Thus, the RTE has to be solved numerically using radiation transport models for spatial and directional dependencies and spectral models for the spectral dependency. One of the radiation transport models is the P1 Radiation Model or the method of Spherical Harmonics. One of the spectral models is the Weighted Sum of Gray Gases Model (WSGGM) that is used to reduce the numerical effort of spectral integration.

When considering coupling radiative transport with the energy equation, the Goulard number Γ determines if this is likely to have an effect [15, p. 24]

$$\Gamma = \frac{2 \times q_{\mathrm{rad}}}{\frac{1}{2} \times \rho_\infty \times u_\infty^3}. \tag{6}$$

If the Goulard number is $>10^{-2}$, radiation is very likely influencing the energy of the flow.

2.1.1 *Governing equations of the P1 radiation model*

One way to simplify the radiative transfer equation (RTE) is the method of Spherical Harmonics. In this method, the radiative intensity is approximated by a two-dimensional Fourier series, splitting the intensity's spatial and directional dependency. If the Fourier series is truncated after one element, the so-called P1 Radiation Model is achieved. In the following parts, scattering of radiation is neglected since production of soot etc. is not considered in this work. For CH_4/O_2 combustion this may not truly be justified since soot is very likely to occur but currently the prediction of soot in the combustion chamber is not as accurate as it should be which in turn would increase the inaccuracy of the follow-up radiative heat transfer simulation.

A detailed derivation of the Spherical Harmonics method can be found in [16, p. 466].

The P1 Radiation Model yields two spatial differential equations, one for the gradient of the directionally averaged intensity G

$$\vec{q}_{\mathrm{rad},\lambda} = -\frac{1}{3 \times a_\lambda} \nabla G_\lambda, \tag{7}$$

and another for the gradient of the radiative heat flux

$$\nabla \vec{q}_{\mathrm{rad},\lambda} = a_\lambda \times (4 \times \pi \times i_{\lambda\mathrm{b}} - G_\lambda), \tag{8}$$

which can be combined to a second-order partial differential equation of elliptic type

$$\nabla\left(\frac{1}{3 \times a_\lambda}\nabla G_\lambda\right) = a_\lambda \times (G_\lambda - 4 \times \pi \times i_{\lambda\mathrm{b}}), \tag{9}$$

that is subject to the boundary condition at a solid wall

$$G_\lambda - \frac{2}{3 \times a_\lambda}\left(\frac{2-\varepsilon_{\lambda\mathrm{w}}}{\varepsilon_{\lambda\mathrm{w}}}\right)\nabla G_\lambda \times \vec{n}_\mathrm{w} = 4 \times \pi \times i_{\lambda\mathrm{bw}}. \tag{10}$$

The P1 Radiation Model has been implemented in the research CFD code NSMB [6] using a local time-stepping algorithm and validated against simple test cases for which analytical solutions are available [7].

2.2 Spectral modeling: Weighted Sum of Gray Gases Model (WSGGM)

Integration of the RTE over wavelength often leads to extreme efforts when using Line-by-Line spectral data because the RTE has to be solved for each spectral line. To overcome this problem, spectral models like the WSGGM are used. Further details on the theory of the WSGGM and some of the up-to-date models can be found in [17]. It was once introduced to simplify the determination of a gas' total emissivity

$$\varepsilon_\mathrm{g} = \sum_{i=0}^{I} w_i(T) \times \left[1 - e^{(-a_i \times S)}\right]. \tag{11}$$

The simplifying approach of the WSGGM is to subdivide the entire spectrum into regions in which the absorption coefficient is assumed to have a constant value a_i. As the absorption coefficient is no longer dependent on the wavelength in this region, it fulfills the requirements of a gray gas, which gives the model its name.

In addition to the gray gases, those regions in the spectrum in which no absorption occurs are represented by a transparent gas denoted by index $i = 0$ with $a_0 = 0$.

In the WSGGM, integration over wavelength is replaced by a weighted sum over the considered gray gases. The total divergence of the radiative heat flux is then the sum of all gray radiative heat flux divergences

$$\nabla \vec{q}_\mathrm{rad} = \int_0^\infty \vec{\nabla}\vec{q}_{\mathrm{rad},\lambda} d\lambda \approx \sum_{i=1}^{I} \nabla \vec{q}_{\mathrm{rad},i}, \tag{12}$$

with I indicating the number of gray gases, or absorption coefficients used.

Each gray gas' divergence in radiative heat flux is given by a modified form of Eq. (2)

$$\nabla q_{\mathrm{rad},i} = a_i \times \left(4 \times w_i \times \sigma \times T^4 - G_i\right), \tag{13}$$

with the blackbody weight w_i indicating the fraction of the entire blackbody spectrum in which the absorption coefficient is a_i

$$w_i = \frac{i_{i,b}}{\int_0^\infty i_\lambda d\lambda} = \frac{i_{i,\mathrm{b}}}{\frac{\sigma \times T^4}{\pi}}. \tag{14}$$

The weights of all gray gases and the clear gas have to fulfill the constraint

$$\sum_{i=0}^{I} w_i(T) = 1. \tag{15}$$

The incident radiation G_i in Eq. (13) is the result of the RTE in Eq. (1), solved with the constant absorption coefficient a_i

$$\nabla\left(\frac{1}{3 \times a_i}\nabla G_i\right) = a_i \times \left(G_i - 4 \times \pi \times w_i \times i_{i,\mathrm{b}}\right). \tag{16}$$

The boundary condition of Eq. (10) becomes

$$G_i - \frac{2}{3 \times a_i}\left(\frac{2-\varepsilon_\mathrm{w}}{\varepsilon_\mathrm{w}}\right)\nabla G_i \cdot \vec{n}_\mathrm{w} = 4 \times w_{i,\mathrm{w}}(T_\mathrm{w}) \times \sigma \times T_\mathrm{w}^4, \tag{17}$$

with the wall's blackbody weight $w_{i,\mathrm{w}}$ and the wall temperature T_w. Note that if the weight is, e.g., a function of temperature, the temperature of the wall has to be used for the wall's blackbody weight.

The WSGG models currently implemented in NSMB are those by Smith [1] for H_2O and H_2O/CO_2 mixtures, Copalle [2] and Johansson [4] for H_2O/CO_2 mixtures and Denison & Webb [18] for H_2O and H_2O/CO_2 mixtures. The first three use a rather simple approach to gain absorption coefficients and weights from total emissivity curve fits whereas the latter model is based on spectral databases.

For mixtures of H_2O and CO_2, the numerical effort remains the same as for single H_2O systems except for the model of Denison & Webb. Whilst the models of Smith, Copalle and Johansson employ an unchanged number of gray gases I for those mixtures (Smith: $I = 3$, Copalle: $I = 3$, Johansson: $I = 4$), there are several options for Denison & Webb's model.

The first option, known as double integration, calculates the mixture absorption coefficients and weights according to

$$\begin{aligned} w_{\mathrm{w,c}} &= w_\mathrm{w} \times w_\mathrm{c} \\ &= \left[F_\mathrm{w}\left(C_{\mathrm{w},j+1}\right) - F_\mathrm{w}\left(C_{\mathrm{w},j}\right)\right] \\ &\quad \times \left[F_\mathrm{c}\left(C_{\mathrm{c},j+1}\right) - F_\mathrm{c}\left(C_{\mathrm{c},j}\right)\right], \end{aligned} \tag{18}$$

$$a_{\mathrm{w,c}} = N_\mathrm{w}\bar{C}_{\mathrm{w},j} + N_\mathrm{c}\bar{C}_{\mathrm{c},j}. \tag{19}$$

The mean absorption cross section of each species is defined as

$$\bar{C}_j = \sqrt{C_j \times C_{j+1}}. \tag{20}$$

The disadvantage of this option is that the number of gray gases and thus the number of equations to be solved is exponentiated, e.g., when using $I = 10$ gray gases for each species, the total number of gray gases becomes $(I + 1) \times (I + 1) = 121$ which is a huge amount of additional computational effort. One possibility to lower the computational efforts is to use less than 10 gray gases per radiating species with the double integration which in turn requires an optimization technique [19]. In this work, reduction to 3 gray gases per species is investigated, leading to a total number of 16 gray gases.

The second option is called convolution approach. In contrast to the double integration, this option needs only I gray gases, similar to the single species system. At first, 10 values for $\bar{C}_{\mathrm{mix},j}$ are defined from which the absorption coefficient is yielded by

$$a_{\mathrm{w,c}} = (N_{\mathrm{w}} + N_{\mathrm{c}}) \times \bar{C}_{\mathrm{mix},j}. \tag{21}$$

The weight is then obtained by subtracting two contiguous blackbody distribution functions

$$w_{\mathrm{w,c}} = \left[F_{\mathrm{mix},j+1}\left(C_{\mathrm{mix},j+1}\right) - F_{\mathrm{mix},j}\left(C_{\mathrm{mix},j}\right)\right], \tag{22}$$

with

$$F_{\mathrm{mix},j}\left(C_{\mathrm{mix},j}\right) = \int_{F_c\left(C_{c,\min}\right)}^{F_c\left(C_{c,\max}\right)} F_w\left(\frac{C_{\mathrm{mix},j} - rC_{\mathrm{c}}}{1-r}\right) dF_{\mathrm{c}}(C_{\mathrm{c}}), \tag{23}$$

$$r = \frac{N_{\mathrm{c}}}{N_{\mathrm{w}} + N_{\mathrm{c}}} \tag{24}$$

and

$$C_{\mathrm{c,max}} = \left(\frac{C_{\mathrm{mix},j} - (1-r)C_{\mathrm{w,min}}}{r}\right). \tag{25}$$

$C_{\mathrm{w,min}}$ and $C_{\mathrm{c,min}}$ are chosen as 3×10^{-5} m^2/mol and $C_{\mathrm{c,max}}$ is set to 60 m^2/mol. The integration of Eq. (23) is carried out with a Gaussian quadrature over 60 intervals. Due to the well-behaved characteristics of $F_{\mathrm{mix,j}}(C_{\mathrm{mix,j}})$ this method is expected to yield a satisfying accuracy with least efforts. The number of intervals has been optimized to 60 within various tests, yielding an error of below 0.5 % to the solution with 1,000 intervals that would lead to much more computational efforts.

The disadvantage of this model is its limitation to systems with a constant mole fraction of species which does not apply to the combustion chambers in this work. The model is therefore used beyond its limitations with variable mole fractions.

The basic idea behind all WSGGM is to allow spectral integration before the RTE is solved. The RTE is then solved for every gray gas separately. To flip the spectral integration and the solution of the RTE is trivial only in homogeneous systems because the wavelengths of occurence of certain absorption coefficients do not change.

Therefore, most WSGG models can be applied only to homogeneous systems with constant temperature, pressure and mole fraction. If the system is not homogeneous, further assumptions have to be made on the way how the wavelengths of occurrence change (in fact it is assumed that they do not) and the simplifications of most WSGG models do no longer hold. To cope with that Denison [5] proposed a model that can be used in nonhomogeneous systems, too. Details on this model can also be found in [12]. The nonhomogeneous model is used in this work in addition to the other WSGG models to estimate the difference in the prediction of the RWHF.

2.3 Numerical method for the basic flow

For the basic flow (velocity, pressure and temperature field, gas properties and composition) inside the considered combustion chambers, Astrium's in-house code Rocflam-II is used [20]. Rocflam-II is an axisymmetric Navier–Stokes solver with a Lagrange droplet tracking module that incorporates several models for multi-class droplet tracking, evaporation and combustion, balancing their accuracy and computational effort. The turbulence modeling is realized via a two-layer k-ε model which switches to a one-equation model for the turbulent kinetic energy near the wall, determining the dissipation ε from an algebraic expression. For the propellant combinations H_2/O_2 and CH_4/O_2, an equilibrium table-based chemistry model is used with a one-dimensional PPDF (Presumed Probability Density Function) approach taking into account the influence of turbulent combustion. No species concentration equations are solved, only a global mixture fraction and its variance are treated by differential equations.

The key of this type of combustion model is the combustion table which is computed separately prior to the computation itself by a chemical equilibrium code [21] and a fluid database [22]. A visualization of the chemistry tables for CH_4/O_2 and H_2/O_2 is given in Fig. 1. Here, the temperature evolution of the combustion between fuel and oxygen is shown as contour on the z-axis and additionally as contour color. On the other axes, the gas solver input quantities mixture fraction f and reduced enthalpy h_{q} are shown. Here, $f = 1$ $(O/F = 0)$ means pure fuel, $f = 0$ $(O/F \to \infty)$ represents pure oxygen. The stoichiometric mixtures of $f \approx 0.2$ $(O/F \approx 4)$ for CH_4/O_2 and $f \approx 0.112$ $(O/F \approx 8)$ for H_2/O_2 are indicated by the red arrows. The enthalpy level of zero corresponds to the injection

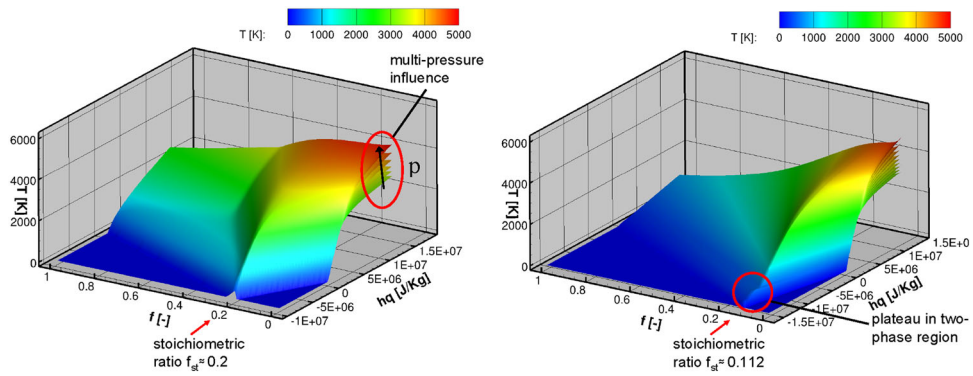

Fig. 1 Multi-pressure equilibrium chemistry table for CH_4/O_2 (left) and H_2/O_2 combustion (right) [25]

temperature of fuel and oxidizer at $f = 1$ and $f = 0$, respectively. Positive enthalpy is related to higher, negative enthalpy is related to lower temperature. At the stoichiometric ratio, the temperature is maximal for the given enthalpy level. It is clearly visible that the combustion temperature increases with increasing enthalpy. The tables are multi-pressure tables which are necessary for a correct description of the flow and the combustion over the entire computational domain including throat and nozzle where the pressure strongly decreases due to flow expansion. The effect of different pressure levels in the table is visible by the multiple contour layers. With increasing pressure, dissociation becomes weaker resulting in a higher temperature at high pressure levels.

3 Calculation strategy

In Fig. 2, the calculation sequence of this work is shown. Based on the Rocflam-II results for temperature, pressure and mole fraction of radiating species which are imported into NSMB, a routine in NSMB calculates the WSGGM

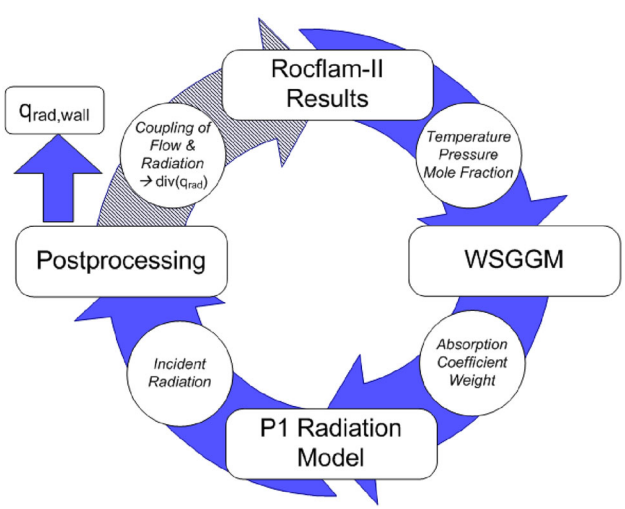

Fig. 2 Calculation sequence for radiative heat transfer analysis

properties absorption coefficient and blackbody weight for each gray gas. These are used as input to the routine that solves the P1 radiation transport model yielding the incident radiation G_i for each gray gas. With a converged solution of the P1 radiation model, postprocessing routines in NSMB construct the RWHF.

As a further option, the divergence of the total radiative heat flux can be used as input to Rocflam-II as a loosely coupled calculation. For loosely coupled simulations, the divergence of the total radiative heat flux, which is the sum over all gray gases, has to be added to the energy equation of Rocflam-II to account for energy transport by radiation, yielding a modified flow field which is then used as input for another radiation simulation. The loose coupling procedure is done until convergence is reached.

To make sure the boundary conditions for radiative heat transfer at the walls of the combustion chambers are properly chosen, the emissivity of the combustion chamber walls has to be determined. The walls of the combustion chambers investigated herein are made of a copper alloy. Emissivity tests for this specific alloy are not available but instead literature sources can be found dealing with the investigation of emissivity for pure copper. A summary of these literature sources can be found in [23, pp. 21–23]. In this work, only the results of Toulukian [24] shall be discussed in detail. Toulukian [24, pp. 136–140] summarizes the emissivity for oxidized copper between 0.5 below 600 K and 0.85 at 1,033 K. Since film cooling at the walls of the combustion chamber is intended to minimize oxidization these emissivities surely are too high with respect to the real conditions in the combustion chambers investigated herein. For polished copper 22 [24, pp. 136–140] states emissivities of 0.017 for low temperatures and 0.05 at nearly 1,200 K. Figure 3 left [23, pp. 23] summarizes the emissivity for oxidized and polished copper as a function of temperature; the temperature at the wall of the combustion chambers is less than 1,200 K for both test chambers and propellant combinations.

One can see that the emissivity strongly depends on oxidization and the temperature of the wall: fully oxidized copper is expected to have the highest emissivity, starting at $\varepsilon = 0.3$

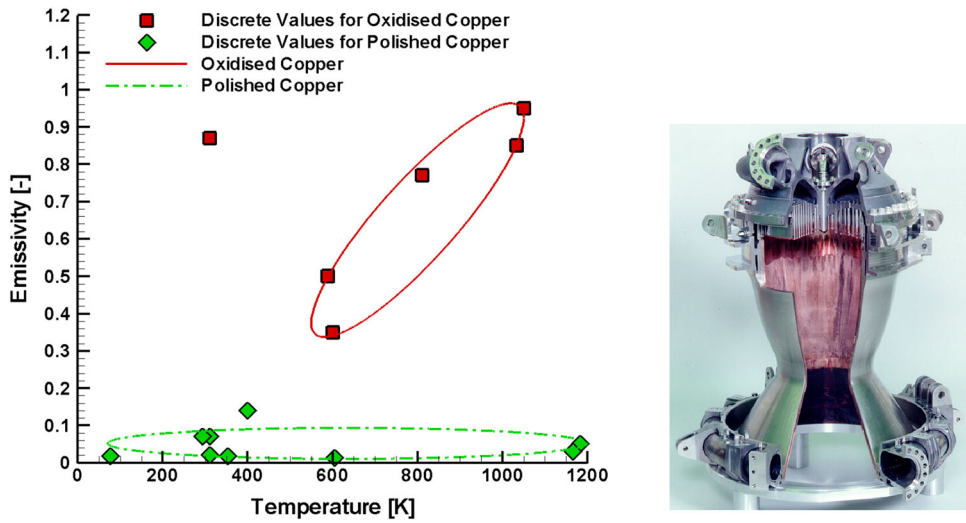

Fig. 3 Surface emissivity versus temperature (left) and picture of a test combustion chamber (right)

at 600 K and ranging up to $\varepsilon = 0.98$ above 1,000 K; in contrast, polished copper does not exceed a maximum emissivity of $\varepsilon = 0.2$. For this work, it is therefore necessary to find a suitable value for the emissivity with regard to a realistic degree of oxidization which is a difficult task.

Upon visual examination of one of Astrium's test combustion chambers, some parts of the chamber are found to be more affected than others. A similar test combustion chamber is displayed in Fig. 3 on the right side. As already mentioned earlier, H_2 film cooling is applied near the wall as additional protection which leads more to a reduction than to an oxidation of the hotgas wall surface. Nevertheless, various regions in the combustion chamber appear dark. In addition, some dull surface regions can be observed which are caused by roughening of the combustion chamber inner surface due to erosion, also leading to an increase of the wall emissivity as compared to a polished surface. To sum it up, it can be stated that an accurate determination of the local wall emissivity necessitates knowledge of several aspects (local combustion gas composition and its effect on surface reduction or oxidation, local wall temperature, local wall surface condition including possible erosion during operation, load point history, …) As such detailed information was not available for every aspect it was chosen to investigate an emissivity range instead of a single emissivity distribution, reaching from values of $\varepsilon = 0.2$ over $\varepsilon = 0.4$ up to $\varepsilon = 0.6$. Each of the three chosen emissivity values of the wall is assumed to be constant along the entire combustion chamber length.

4 H_2/O_2 combustion

For the H_2/O_2 combustion two different geometries are investigated, a subscale and a fullscale chamber, as shown in Fig. 4. The subscale design has been chosen in a way that it is representative for fullscale in terms of heat load on the wall as well as characteristic length and thus propellant preparation and evaporation. The smaller dimensions of the subscale hardware make it possible to experimentally gather detailed calorimetric heat flux measurements at reduced complexity and costs. The calorimetric measurements are realized by computing the enthalpy difference between inflow and outflow of the multiple individual segments on the basis of temperature, pressure as well as velocity differences. The comparison of these data to the Rocflam-II simulation is presented in Fig. 5.

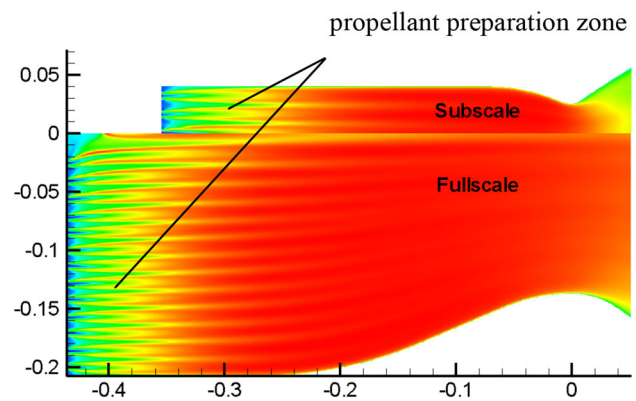

Fig. 4 Temperature contours of subscale and fullscale combustion chamber for H_2/O_2 combustion

It becomes visible that the overall agreement between simulated and measured local heat flux is very good. A small deviation can be observed in the injection area near the face plate, where the simplification of axisymmetry has its strongest influence. Both, the temperature plot in Fig. 4 as well as the heatflux profile in Fig. 5 display the propellant preparation zone which has not been resolved in

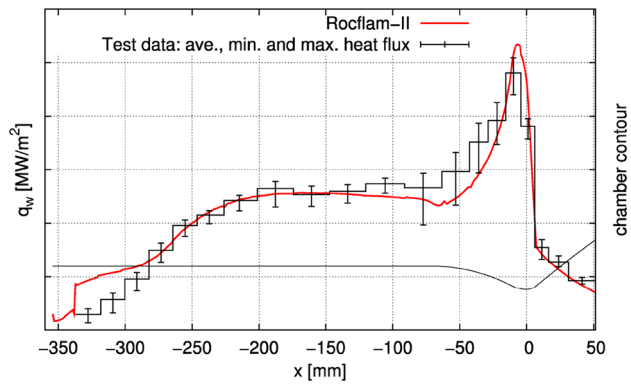

Fig. 5 Local heat flux profiles of simulation and experiment for the H_2/O_2 subscale chamber

former studies [10, 17] providing combustion efficiency lower than unity and a thermally less loaded region close to the injector. The load point (chamber pressure and mixture ratio) for which the comparison is shown is the one of the fullscale chamber. Concerning geometrical similarity, the photo-scaling principle is applied for the generation of the subscale chamber. This leads to a shorter convergent combustion chamber section compared to fullscale (see Fig. 4), locally generating a higher axial pressure and hence also temperature gradient. Nevertheless, it is expected that the local convective heat flux prediction presents a realistic evolution also for fullscale. This is confirmed by the good agreement of the integral heat load between simulation and experiment for the fullscale chamber. There, the measurement of the integral heat load is realized by a single calorimetric measurement between inlet and outlet of the cooling circuit.

The results in RWHF for both the subscale and fullscale combustion chamber using different wall emissivities can be seen in Fig. 6. The plots are normalized with the maximum CWHF of the corresponding combustion chamber. The left and the right scale of each diagram in Fig. 6 differ by two orders of magnitude; at intersections of RWHF and CWHF the former is 1 % of the latter. In addition, the radially averaged temperature is shown in Fig. 6.

First, one can see that the RWHF evolves with increasing temperature depending on its fourth power. As Fig. 6 underlines, the cross-sectionally averaged temperature increases as chemical reactions take place, reaching its maximum shortly upstream of the throat. The RWHF also has its maximum near that position: In the subscale combustion chamber, the maximum RWHF is located slightly upstream (−0.111 m) of the maximum temperature (−0.072 m) having a difference of 39 mm. In the fullscale chamber, the maximum temperature lies at −0.169 m and the maximum RWHF is at −0.197 m so the difference is 28 mm. Compared to the total dimensions of the chambers the distance between the positions of maximum temperature and RWHF is below 8.6 and 5.6 % of the total chamber length. The reason for the slight difference of the maximum positions is that the radially averaged temperature has a different maximum position than those specific regions in radial direction that influence the RWHF most through their emission. Downstream of the throat the RWHF decreases rapidly with the expansion of the flow diminishing the temperature. One can see the different decreasing characteristics between the subscale and fullscale chambers downstream of the throat as the RWHF has a steeper slope in the subscale chamber. According to Fig. 6, the averaged temperature decreases more rapidly in

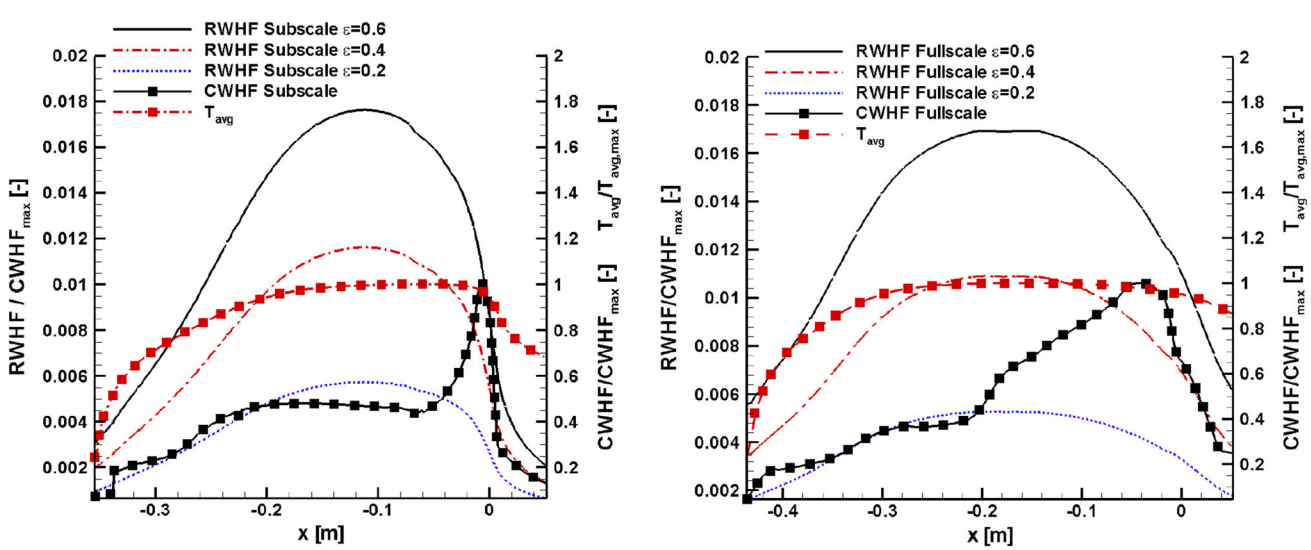

Fig. 6 Normalized CWHF, RWHF and averaged temperature for Denison's WSGGM (homogeneous systems) for subscale (left) and fullscale (right) combustion chamber using different wall emissivities

the subscale chamber, causing the RWHF to drop off steeper than in the fullscale chamber. This is linked to the fact that at equivalent nozzle length the expansion ratio of subscale is much higher than for fullscale.

Second, the influence of the wall emissivities becomes obvious in Fig. 6. With an emissivity of $\varepsilon = 0.6$, the normalized RWHF reaches its maximum of 0.0176 in the subscale and 0.0169 in the fullscale chamber. At $\varepsilon = 0.4$, it is 0.0116 and 0.0108 and with an emissivity of $\varepsilon = 0.2$ it reaches the smallest values of 0.0057 and 0.0052. Thus, the decrease in maximum RWHF is linear to the decrease in the emissivity of the wall. For the considered combustion chamber material the values can range from $\varepsilon \approx 0.1$ for the polished case up to $\varepsilon \approx 0.8$ for oxidized conditions. Thus, a value of $\varepsilon = 0.6$ represents a high but realistic choice, all the more when considering already aged chambers.

Third, Fig. 6 shows the different length of the high RWHF zones which are broader in the fullscale combustion chamber. This difference is due to the temperature inside the chambers as Fig. 6 underlines in terms of the averaged temperature. Because of the increased length of the fullscale combustion chamber, the high temperature regions inside this chamber are longer than in the subscale combustion chamber showing a significant region of constant maximum temperature that in turn results in a broadening of the associated high RWHF zones.

The results for the different WSGG models used in the H_2/O_2 combustion, namely the homogeneous ones by Smith and Denison and the nonhomogeneous model by Denison, are shown in Fig. 7. In the subscale chamber, both homogeneous WSGG models predict nearly the same ascent of the RWHF upstream of the throat as well as nearly the same maximum RWHF. Downstream of the throat, the difference between both models increases. The location of the maximum RWHF is slightly shifted by 30 mm with the maximum predicted by Denison's model being upstream of the prediction by Smith's model. The nonhomogeneous model by Denison predicts a smaller RWHF, reaching a maximum of only 72 % of the other's RWHF. Nevertheless, the overall behavior as well as the location of the maximum RWHF is predicted equally. The differences between the homogeneous and nonhomogeneous WSGGM vanish downstream of the throat indicating that nonhomogenities in the flow are reduced. Figure 4 shows that the temperature field in both chambers is less stratified shortly upstream of the throat and the flow is more uniform so the use of nonhomogeneous WSGGM does not yield any significant advantage over the simple homogeneous models.

For the fullscale chamber, the difference between models increases as Smith's model predicts a smaller RWHF than Denison's homogeneous WSGGM. The difference in maximum RWHF is around 20 %. The location of the maximum RWHF is predicted equally by both models at −0.15 m. The nonhomogeneous WSGGM by Denison predicts also a smaller RWHF in the fullscale chamber, reaching a maximum of 75 % of the homogeneous model. It is only a coincidence that Smith's WSGGM predicts a maximum RWHF that is close to the one by Denison's nonhomogeneous model. One has to note that in contrast to the RWHF in the subscale chamber, the RWHF at the injector faceplate predicted a lot smaller in the fullscale chamber by the nonhomogeneous WSGGM, which might have an influence on the local ratio of RWHF to TWHF.

Since the difference in maximum RWHF predicted by the two homogeneous WSGGM does not occur in the subscale chamber, the size of the combustion chamber seems to be responsible for that. In former investigations of

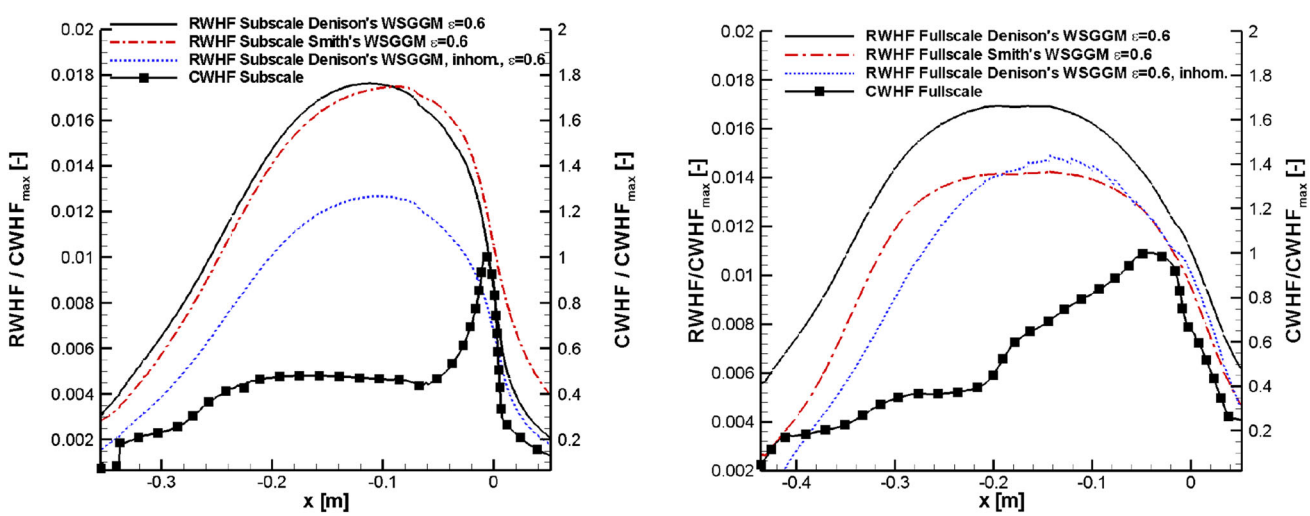

Fig. 7 Comparison of normalized RWHF for Denison's and Smith's WSGGM for subscale (left) and fullscale combustion chamber (right)

the space shuttle main engine [10, p. 73], whose dimensions are comparable to that of the fullscale chamber in this work, the WSGGM by Denison also predicted the highest RWHF as compared to the simple model by Smith. With an increased dimension, especially with an increased diameter, the path length for radiative heat transfer increases and according to Eq. (11), the product of absorption coefficient and path lengths grows leading to a higher emissivity. Since Denison's model has a more profound theoretical basis than Smith's model, it is concluded that absorption is more precisely modeled in that model while Smith's model underestimates the absorption coefficient along the path, reducing the emissivity and leading to a lower maximum RWHF. The differences become obvious only in the fullscale chamber whose diameter is about 5 times the diameter of the subscale combustion chamber; the path lengths in the subscale chamber are obviously too low to cause any significant difference in maximum RWHF.

Figure 8 finally summarizes the local ratio of RWHF to TWHF for both combustion chambers at a constant wall emissivity. Due to the different lengths of both combustion chambers the abscissa is normalized so the position of the faceplate equals zero and the throat is at 1.0. For $\varepsilon = 0.6$, the maximum local ratio of RWHF to TWHF is nearly 10 % in the fullscale chamber and 9 % in the subscale chamber using a WSGGM for homogeneous media. Using a WSGGM for nonhomogeneous media, the maximum ratio is only 5 % in the subscale and 3 % in the fullscale chamber. The level of maximum ratio is subject to the WSGGM used. Thus, the WSGGM for nonhomogeneous media reduces the maximum ratio of RWHF to TWHF further.

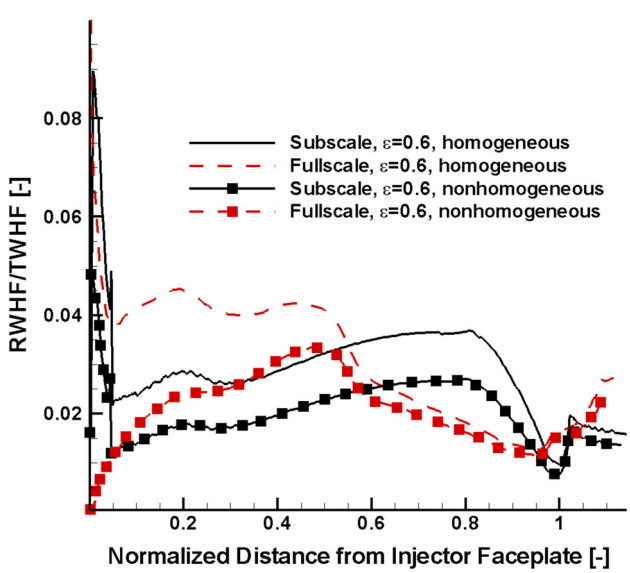

Fig. 8 Local influence of RWHF on the TWHF for H_2/O_2 combustion with Denison's WSGGM for homogeneous and nonhomogeneous systems

In both chambers, the maximum ratio occurs shortly downstream of the injector faceplate when a homogeneous WSGGM is used. The main reason for that is the low CWHF at the injector faceplate. Although the RWHF is also lowest at the inlet, the small CWHF causes the ratio of both to increase. When using a nonhomogeneous WSGGM the maximum ratio is still at the injector faceplate for the subscale chamber but for the fullscale chamber it occurs further downstream. This is caused by the RWHF as shown in Fig. 7. The ratio based on the homogeneous model matches the one based on the nonhomogeneous model upstream of the throat. As mentioned before, this is an indication that inhomogeneities decrease when the flow passes the throat of the combustion chamber.

The above results confirm the assumption that some points along the wall are more influenced by radiation than others. Nevertheless, the critical regions near the throat are not influenced significantly by the RWHF as the local ratio there is lower than 2 %, especially for the fullscale chamber and with the nonhomogeneous WSGGM.

In Table 1, the integrated ratios of RWHF to TWHF are summarized. Again, one can recognize the influence of the wall emissivity on the results. The integrated ratio decreases linearly by nearly one percentage point in the subscale chamber for an emissivity decrease of 0.2. In the fullscale chamber the decrease is slightly lower. For the subscale combustion chamber, Table 1 underlines that there is nearly no difference in the prediction of both homogeneous WSGG models. Using the nonhomogeneous WSGGM yields an integrated ratio of nearly 2 % in the subscale chamber.

In the fullscale chamber, the prediction of the integrated ratio of RWHF to TWHF differs for both homogeneous WSGG models. Denison's model yields the highest ratio due to its prediction of the highest RWHF in the fullscale chamber. With Denison's nonhomogeneous WSGGM, the integrated ratio is also nearly 2 %.

Table 1 Integral ratio of RWHF/TWHF for all WSGG Models, wall emissivities and chamber sizes for H_2/O_2 combustion

	RWHF/TWHF (%)		
	$\varepsilon = 0.6$	$\varepsilon = 0.4$	$\varepsilon = 0.2$
Subscale chamber			
Smith's WSGGM	2.98	1.91	0.94
Denison's WSGGM, homogeneous	2.94	1.95	0.97
Denison's WSGGM, nonhomogeneous	2.02	–	–
Fullscale chamber			
Smith's WSGGM	2.54	1.66	0.82
Denison's WSGGM, homogeneous	3.30	2.10	1.00
Denison's WSGGM, nonhomogeneous	2.08	–	–

The reason for the difference between homogeneous and nonhomogeneous WSGGM is in the greater accuracy of the latter model. With the nonhomogeneous model, absorption due to hot lines occurring at high temperatures is modeled more precisely which in turn decreases the RWHF.

4.1 Investigation of coupling between radiation and the flow

The calculation scheme of Fig. 2 allows the coupling of radiation to the energy equation of the flow solver. Coupling is investigated in this work for H_2/O_2 combustion in the subscale chamber in a loose manner, meaning that only the converged divergence of radiative heat flux of NSMB, taken from Eq. (12) using the WSGGM, is imported into Rocflam-II which then computes a new flow field that is then again imported into NSMB to obtain a new radiation field. This is done until an overall convergence is reached and both flow and radiation fields do no longer change significantly. Radiation coupling in this work does not involve the transfer of the radiative wall heat flux because the temperature at the combustion chamber walls is kept constant based on experimental results and is not subject to an energetic boundary condition.

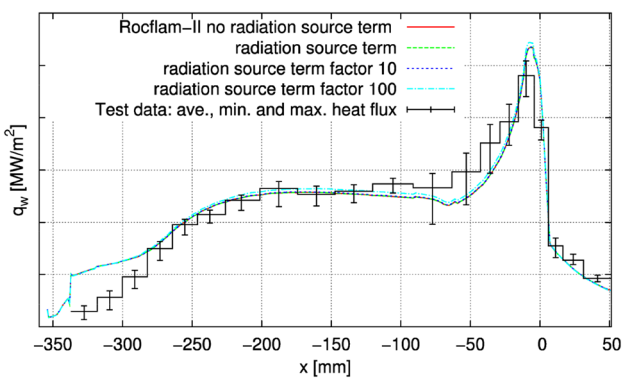

Fig. 9 Influence of radiation coupling on the normalized CWHF for the subscale chamber for H_2/O_2 combustion

The results of the coupling are shown in Fig. 9 for the CWHF and in Figs. 10 and 11 for the radial temperature profile. It is obvious that coupling the divergence of radiative heat flux into the energy equation has negligible influence on the CWHF. One can depict no difference between the original CWHF, the CWHF gained with the divergence of radiative heat flux coupled into the energy equation and the CWHF in case the divergence of radiative heat flux of NSMB is artificially increased by a factor of 10. Only if the divergence of radiative heat flux is amplified by a factor of 100, small disturbances of the original CWHF can be seen whereas these occur only near the throat whereas the CWHF at the injector faceplate is not influenced at all.

Concerning the evolution of radial temperature Fig. 10 shows similar results. At all axial locations, there are no differences in both the entire radial temperature profile as well as in the zoomed temperature profile near the wall.

Differences in radial temperature profiles occur first if the divergence of radiative heat flux is amplified by a factor of 100, as shown in Fig. 11. As with the CWHF, the strongest influence occurs near the throat while the region near the injector faceplate is not influenced by radiation. The reason why radiation influences the near-throat regions more than those at the injector faceplate is the incident radiation which increases similar to the RWHF with temperature, having its maximum shortly upstream of the

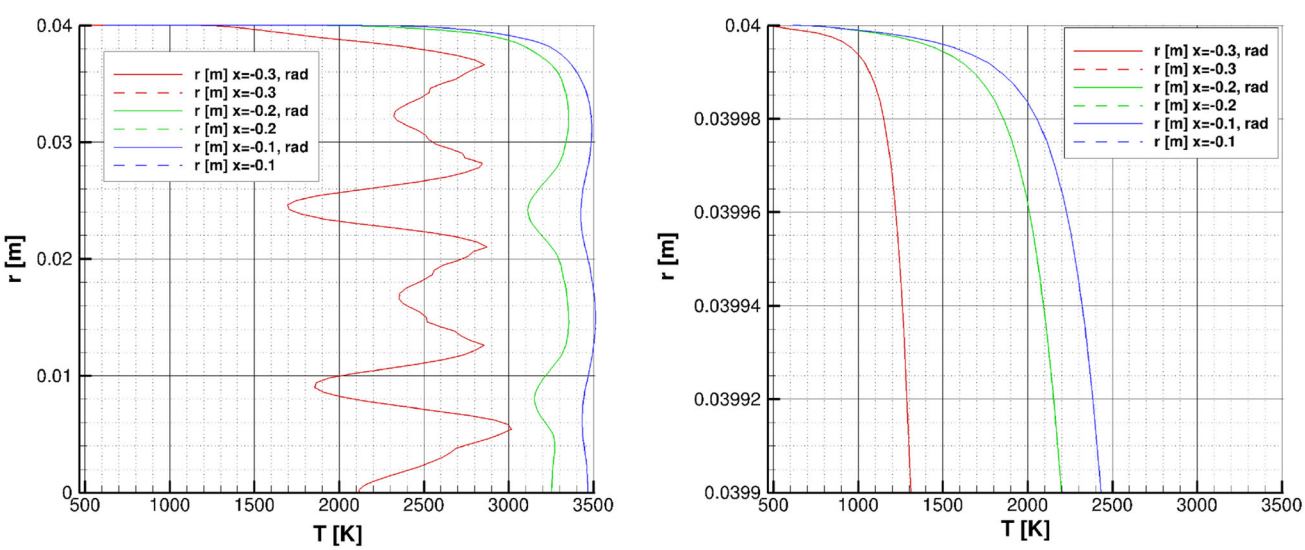

Fig. 10 Influence of radiation coupling on the radial temperature profile for the subscale chamber for H_2/O_2 combustion

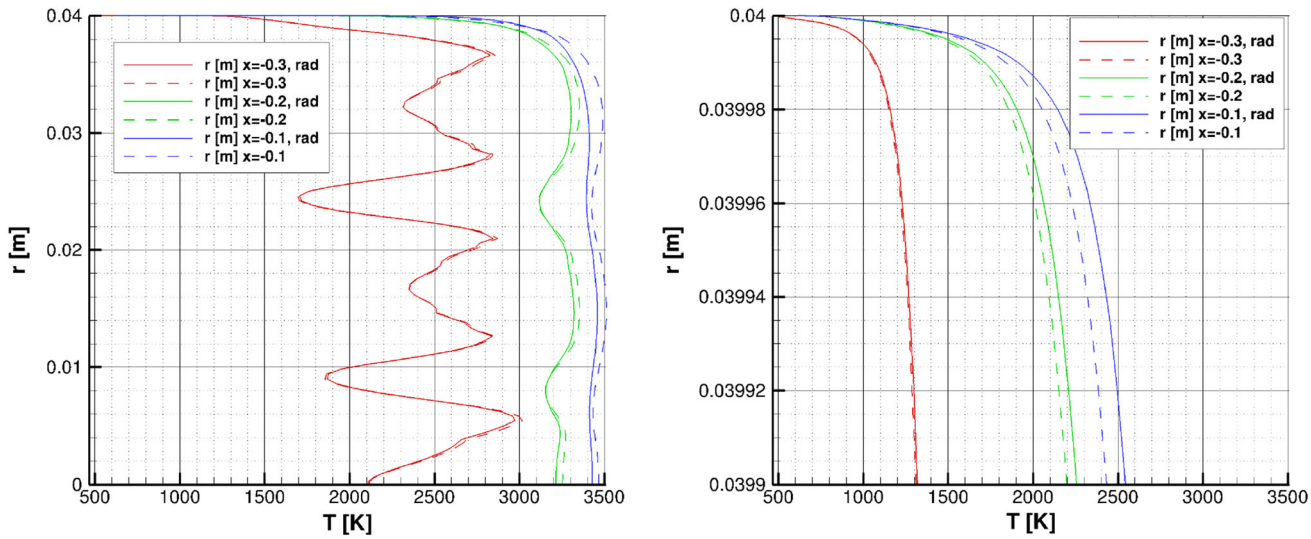

Fig. 11 Influence of radiation coupling on the radial temperature profile for the subscale chamber for H_2/O_2 combustion when amplifying the divergence of radiative heat flux by a factor of 100

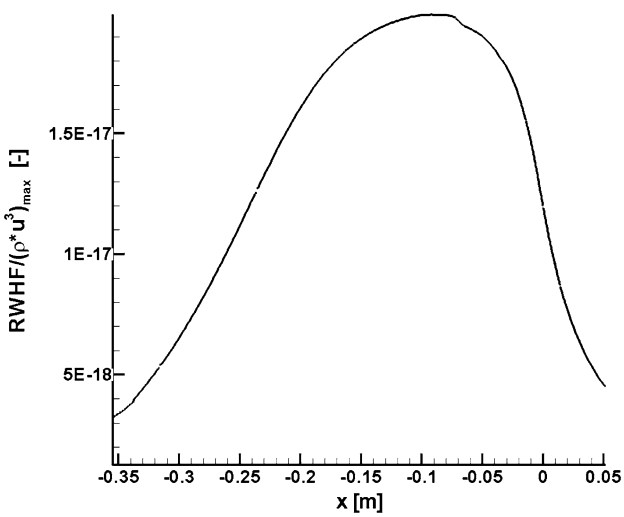

Fig. 12 RWHF for Smith's WSGGM normalized with internal energy of the flow versus axial distance

throat where the convergent section begins. Therefore, the divergence of radiative heat flux in which the incident radiation is included, has its maximum there too, influencing the energy equation of the flow there most.

The results concerning the influence of radiation on the temperature profile are similar to those presented in a former investigation [10]. In that work, the investigation of radiative transfer in SSME Main Combustion Chamber revealed no significant difference in the radial temperature profile when radiation was considered. Figure 12 shows the RWHF of the subscale chamber normalized by internal energy next to the wall, needed for the Goulard number of Eq. (6).

One can see that the internal energy outranges the RWHF by 16 orders of magnitude, so the Goulard number is in the order of 10^{-16} leading to a negligible influence of radiation on the flow which is confirmed by the results shown in Figs. 9 and 11.

The results above are all gained in only one loose coupling step meaning that the divergence of radiative heat flux is imported in Rocflam-II only once as it becomes obvious that both temperature and CWHF do not change.

4.2 Influence of the volume on the radiative wall heat fluxes

Using the results for both subscale and fullscale combustion chambers for H_2/O_2 combustion, the influence of the combustion chamber dimension on the RWHF is investigated. Figure 13 shows the RWHF for the two chamber sizes at various wall emissivities, using two different WSGG models, normalized with the absolute maximum of RWHF at $\varepsilon = 0.6$. The operating conditions in the subscale (photoscaled) and fullscale combustion chamber are identical, making their results comparable.

The maximum RWHF is predicted independent of the chamber volume when using the WSGGM by Smith as both chambers have nearly the same maximum RWHF; the maximum difference is 3 % for $\varepsilon = 0.6$. In contrast, using Denison's WSGGM yields a different result especially for an emissivity of $\varepsilon = 0.6$ resulting in the highest difference between the subscale and fullscale result in RWHF of 18 % with the higher RWHF in the fullscale chamber. For decreasing emissivities, this difference lowers to 15 % ($\varepsilon = 0.4$) and 14 % ($\varepsilon = 0.2$) but is still far greater than with Smith's WSGGM. As discussed above, the WSGGM by Denison is known to be more accurate than the one by

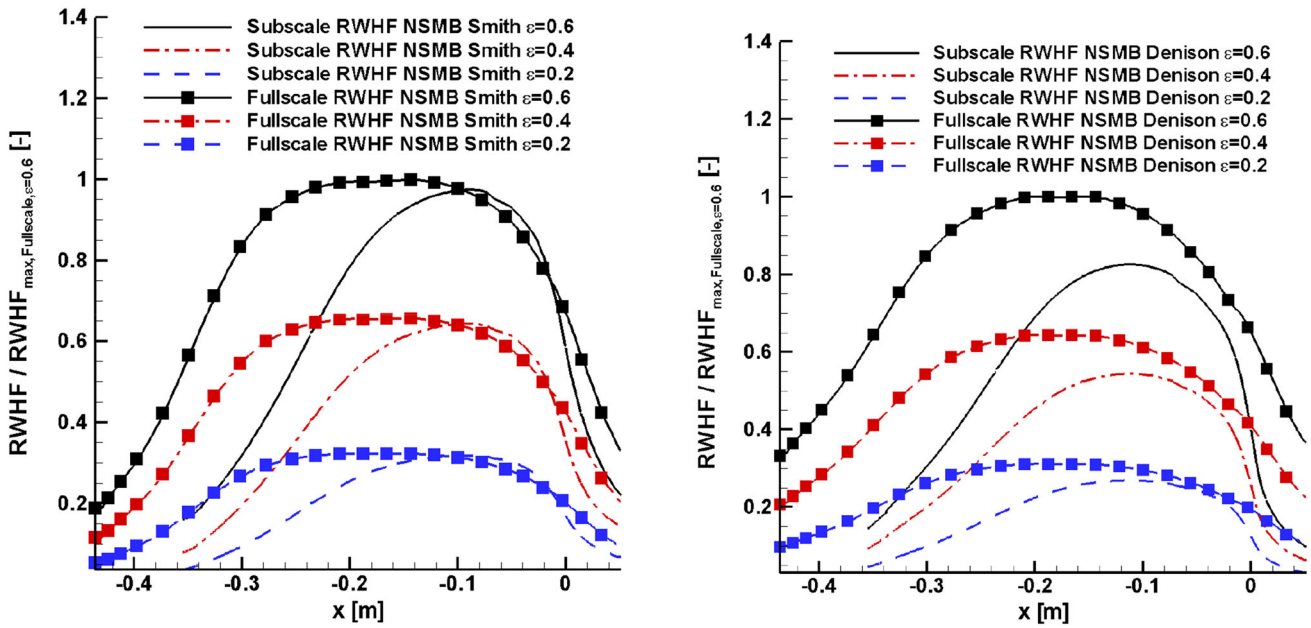

Fig. 13 Differences in RWHF between subscale and fullscale chambers for H_2/O_2 combustion for two homogeneous WSGG models by Smith (left) and Denison (right)

Smith. As seen in the previous section, differences between both WSGG models occur only at greater path lengths as they are encountered in the fullscale chamber. Thus, the prediction of the RWHF by Smith's WSGGM is assumed to be too low (compare Fig. 7) resulting in a vanishing difference in the RWHF between the fullscale and subscale chamber as shown in the left of Fig. 13.

In addition, the results on the right side of Fig. 13 match simple predictions that can be made using Eq. (11), such as: with bigger volume, the path length grows, too. With the product of absorption coefficient and path length the emissivity of the gas increases and so does the emission and RWHF in the fullscale chamber. Although Eq. (11) is valid only under the assumption of a constant absorption coefficient, it seems suitable as a rule of thumb.

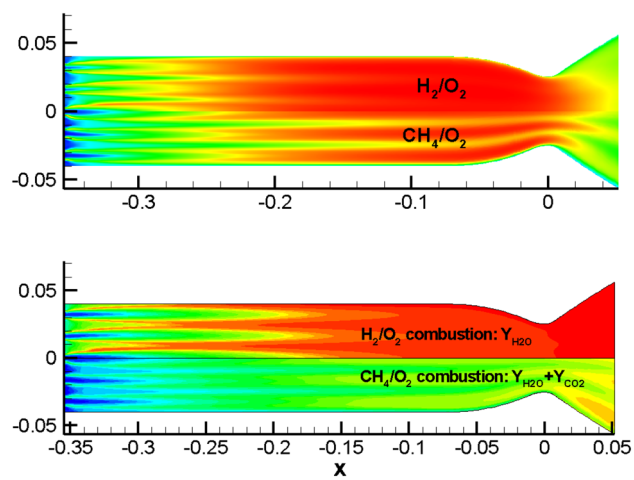

Fig. 14 Temperature contours (top) and contours of mass fractions of the radiation-relevant species (bottom) in the subscale combustion chamber for H_2/O_2 and CH_4/O_2 combustion

5 CH_4/O_2 combustion

Concerning the basic flow, significant differences can be observed between hydrogen and methane combustion as Fig. 14 underlines. First of all, looking at the temperature on top of Fig. 14, it appears that the flame zone within the chamber starts farther downstream for methane than in the case of hydrogen. Furthermore the stratification in the throat area is higher for CH_4/O_2 combustion. Both effects are mainly driven by the different droplet size distributions of the two propellant combinations.

In addition, by looking at the bottom of Fig. 14 one observes that the sum of mass fractions for H_2O and CO_2 is perceptibly lower in the case of methane than it is for H_2O in the pure hydrogen combustion. This is surprising at first sight but results from the fact that a substantial part of the exhaust gas contains CO which is produced at high temperatures. However, CO is not considered in the radiative transfer calculation since the WSGG models used herein do not support it. Figure 15 indicates that neglecting CO is justified for atmospheric conditions where its maximum intensity is around 10 % of the intensity of CO_2 and around 13 % of water's intensity.

Nevertheless, at high-temperature and high-pressure conditions as in rocket combustion chambers, neglecting

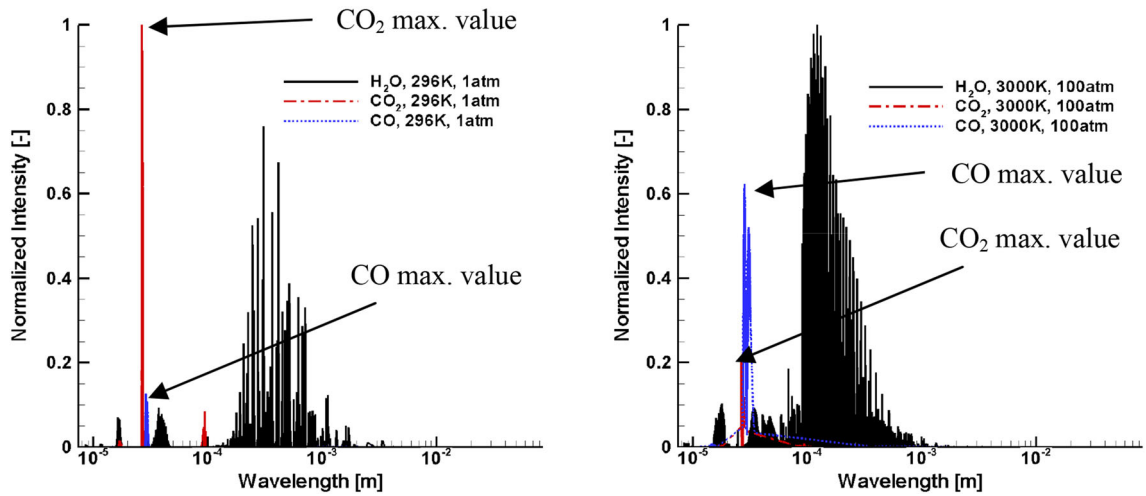

Fig. 15 Spectral intensity from HITRAN for H_2O, CO_2 and CO at atmospheric conditions (left) as well as at combustion chamber conditions (right)

CO for radiative transfer is not justified. One can see that the maximum intensity of CO is even greater than the intensity of CO_2 reaching about 60 % of the intensity of H_2O.

Thus, not considering the contribution of CO to the radiative transfer introduces an error to the accuracy of the simulation. Its order of magnitude may be similar to the influence of CO_2 on the radiative transfer because the spectral occurrences of both lines are very similar. This results in nearly the same spectrally integrated intensity, representing the emission of those lines. From Fig. 15, one can estimate that the influence of CO_2 and CO is marginal as compared to H_2O which has a lot broader line distribution, increasing the emission from those lines. Detailed quantitative predictions of the influence on CO cannot be made since CO is not considered in any of the spectral models used in this work.

A comparison of the locally measured heat flux for the CH_4/O_2 case in Fig. 16 shows that the general agreement with the simulation is as good as in the case of H_2/O_2.

Concerning the general evolution of the heat flux profiles it should be mentioned that the applied propellant injection method is slightly different for both propellant combinations, leading to a negligible steeper heat flux gradient in proximity of the faceplate compared to the H_2/O_2 case. More important than the injection method is the load point equivalence between the two propellant combinations. Therefore, the chamber pressure for both cases is kept constant. Due to the different stoichiometric ratios of H_2/O_2 (≈ 8) and CH_4/O_2 (≈ 4) combustion the absolute value of the mixture ratio could not be kept. However, based on the available experimental data the best possible relative match to the hydrogen case was chosen. Finally, the resulting combustion temperature assuming equilibrium is about

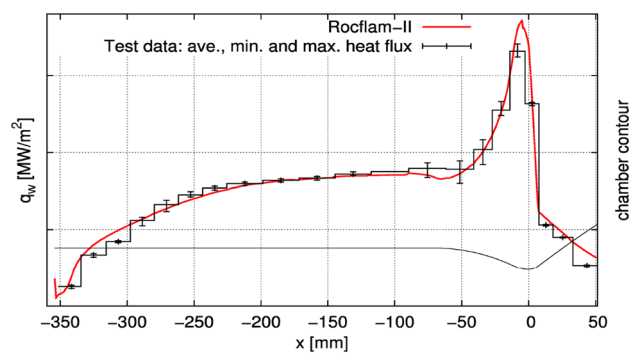

Fig. 16 Local heat flux profiles of simulation and experiment for the CH_4/O_2 Subscale chamber

40 K lower for the methane configuration, which has to be kept in mind when comparing the results.

The left side of Fig. 17 shows the normalized RWHF in comparison with the CWHF for different wall emissivities using Smith's WSGGM. Similar to the H_2/O_2 case the scales of both axes differ by approximately 2 orders of magnitude. The maximum RWHF in case of the CH_4/O_2 simulation is 1.65 % of the maximum CWHF which is slightly lower than in the H_2/O_2 simulation. The reason for that is on the one hand the decreased temperature of the CH_4/O_2 combustion load point and on the other hand the sum of mass fractions of H_2O and CO_2 which is lower than the mass fraction of pure H_2O in the H_2/O_2 combustion as Fig. 14 underlines. Taking CO into account in the spectral modeling would increase the ratio for CH_4/O_2 combustion. The maximum RWHF lies 43 mm upstream of the maximum temperature which is a difference of 11 % of the total chamber length and comparable to the difference between both maxima in the H_2/O_2 combustion.

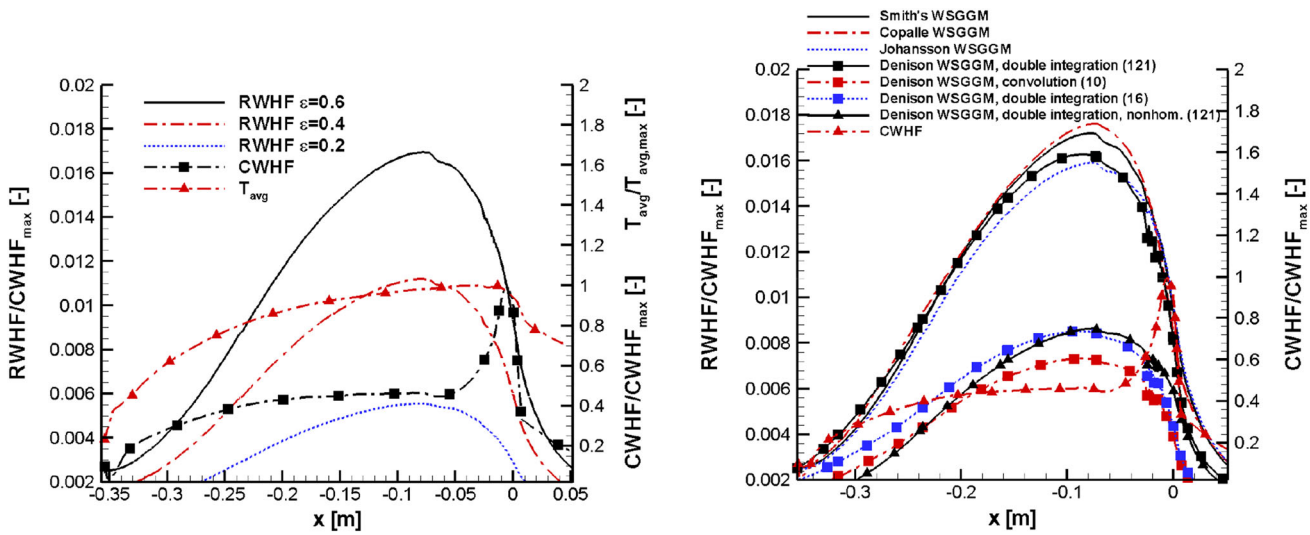

Fig. 17 Comparison of normalized CWHF and RWHF for Smith's WSGGM using different wall emissivities (left)and of normalized RWHF for various WSGG Models for Subscale CH_4/O_2 combustion ($\varepsilon = 0.6$) (right)

With varying wall emissivity, the normalized RWHF decreases from 0.0165 at $\varepsilon = 0.6$ to 0.0111 at $\varepsilon = 0.4$ and reaches its lowest value of 0.0055 with $\varepsilon = 0.2$. Thus, the decrease in maximum RWHF with emissivity is linear like it is in the H_2/O_2 case.

The differences in RWHF for the different WSGG models are shown on the right side of Fig. 17. Besides the simple model for homogeneous systems by Smith several other models are used for mixtures of H_2O and CO_2. These are models by Copalle and Johansson. All three simple WSGG models predict almost the same ascent and descent of RWHF whilst there is only a small difference in the prediction of the maximum RWHF. The position of the maximum RWHF does not differ significantly between those three models and varies between −0.09 m and −0.07 m which is a difference of 5 % relatively to the length of the chamber.

In addition, the WSGGM for homogeneous media by Denison using 121 gray gases with the double integration (whose origins are in the use of 10 gray plus 1 transparent gas for each species, thus $11 \times 11 = 121$ gases) is in accordance with the three simple models mentioned above. It matches Johansson's results best from the injector down to the throat but differs from the three simple models in the expansion region.

The simplified options for Denison's homogeneous WSGGM predict the lowest RWHF that is only half of the other ones' RWHF reaching 0.7 % of the maximum CWHF. A possible reason for the lower prediction of the RWHF with the convolution option is the option's limitation to constant mole fractions which is violated herein. The reason for the lower prediction of Denison's model based on double integration with optimized intervals is that the optimization algorithm yields only one of various local minima instead of the global one. Therefore, the results of the three simple models and of Denison's model using 121 gray gases appear more trustworthy since they have neither limitations that are exceeded nor the necessity of optimization.

With the nonhomogeneous model of Denison using 121 gases in a double integration, the RWHF decreases to 53 % of the homogeneous model's prediction. This decrease in RWHF is in line with the RWHF decrease of the H_2/O_2 combustion shown in the previous chapter: assuming that the decrease in RWHF for pure CO_2, due to the nonhomogeneous modeling, is similar to the one for H_2O (which is 25 %, when using the nonhomogeneous model) the RWHF of the mixture is $(75\ \%)^2 = 56\ \%$ of the RWHF predicted by the homogeneous model. This approach is justified since in the double integration, the emission power (represented by the blackbody weight) of the mixture is obtained by multiplication of both species' emission powers (see Eq. 16). As the decrease in RWHF for pure CO_2 may not be exactly the same as for H_2O, the above prediction deviates from the results in NSMB by three percentage points. Due to the high numerical effort, the nonhomogeneous WSGGM is used only for one emissivity of $\varepsilon = 0.6$.

The local ratio of RWHF to TWHF for two homogeneous and one nonhomogeneous WSGGM at $\varepsilon = 0.6$ is shown in Fig. 18. One can see that the plot is similar to the one for H_2/O_2 combustion in the subscale chamber shown in Fig. 8 where the maximum ratio occurs close to the injector. The quantitative level of the ratio of RWHF to TWHF is slightly lower in the CH_4/O_2 case reaching a maximum of only 8 % in contrast to 10 % in the H_2/O_2 case when using the

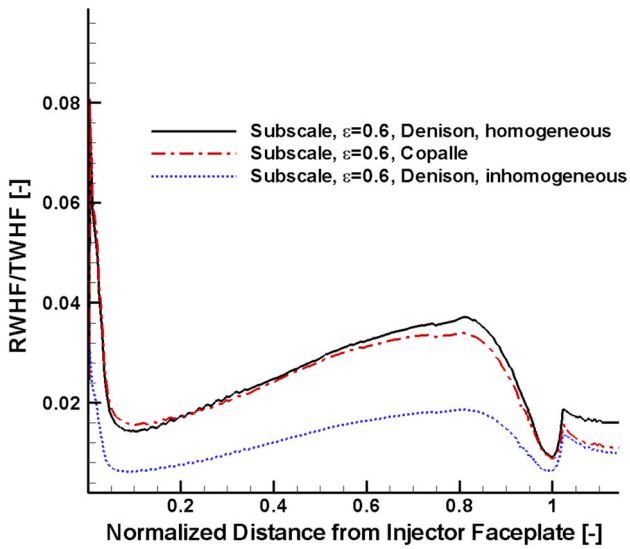

Fig. 18 Local influence of RWHF on the TWHF for CH_4/O_2 combustion

Table 2 Integral ratio of RWHF/TWHF for all WSGG Models and wall emissivities for CH_4/O_2 combustion

	RWHF/TWHF (%)		
	$\varepsilon = 0.6$	$\varepsilon = 0.4$	$\varepsilon = 0.2$
Subscale chamber			
Smith's WSGGM	2.49	1.66	0.83
Copalle's WSGGM	2.55	1.69	0.85
Johansson's WSGGM	2.37	1.55	0.76
Denison's WSGGM (double integration, 121 gases)	2.42	–	–
Denison's WSGGM (double integration, 16 optimized gases)	1.40	0.94	0.47
Denison's WSGGM (convolution, 10 gases)	1.18	0.78	0.39
Denison's WSGGM (double integration, 121 gases, nonhomogeneous)	1.27	–	–

homogeneous WSGGM. With Denison's nonhomogeneous model, the maximum local ratio is 3 %, similar to the H_2/O_2 combustion in the subscale chamber but with a different location at the injector faceplate.

For the CH_4/O_2 combustion Table 2 shows the integrated ratio of RWHF to TWHF for all WSGG models and emissivities. Similar to the RWHF, the integrated RWHF/TWHF is nearly the same for the WSGG models by Smith, Copalle and Denison predicting a maximum ratio of $\sim$2.5 % at $\varepsilon = 0.6$ which is about a half percentage point lower than that in the H_2/O_2 combustion. For these three models a decrease in emissivity by 0.2 decreases the ratio by 0.8 percentage points. This linear behavior is very similar to the one in the H_2/O_2 combustion. The homogeneous WSGGM by Denison using the double integration option with 121 gray gases yields similar results for $\varepsilon = 0.6$; the other emissivities are left out in this work due to the extremely high computational efforts of this method. Nevertheless it can be assumed from the results of the H_2/O_2 combustion and from the performances of the other WSGG models in the CH_4/O_2 combustion that the reduction per emissivity is comparable.

The integrated ratio gained by the simplified options of Denison's homogeneous WSGGM is only half of the prediction by the other models because their RWHF shows only half of the other's as well. Nevertheless, with decreasing emissivity these models behave very similar. Finally, when using the most accurate nonhomogeneous WSGGM, the integrated ratio decreases to 1.27 %.

6 Comparison of results to former investigations

The findings of this work contradict the results of former investigations of radiative heat transfer in the space shuttle main engine (SSME) Main Combustion Chamber (MCC) with respect to the predicted integral ratio of RWHF to TWHF [10, 11] which was found to be 7.7 % for H_2/O_2 and 8.8 % for CH_4/O_2 combustion.

The main difference to the investigation of the SSME MCC lies in the simulation of the combustion chamber flow which has been predicted for the SSME MCC assuming a pre-burnt equilibrium mixture of fuel and oxidizer entering the domain. This resulted in very high temperatures shortly behind the injector face plate, causing the RWHF to start at a very high level as Fig. 19 shows for H_2/O_2 combustion.

To achieve a throat heat flux level comparable to the former SSME investigation an unusual high load point was chosen for the fullscale chamber. The result in Fig. 19 shows that the temperature for H_2/O_2 combustion increases smoothly from the inlet where it is only 70 % of the SSME's temperature. The RWHF of the fullscale combustion chamber at the inlet is only 20 % of the RWHF for the SSME which has its maximum there. Besides the temperature that differs by 30 % causing the emission to drop by nearly 75 % ($\sim T^4$), the mass fraction of H_2O is the other influential factor: in the SSME, the maximum mass fraction of H_2O is 94 % occurring at the inlet due to the equilibrium composition entering the domain [10, p. 60]. In the fullscale combustion chamber, the maximum mass fraction at the inlet is below 20 % and increases toward the throat as reactions occur. Thus, in the fullscale combustion chamber, the lower temperature as well as the lower mass fraction of H_2O reduces the RWHF.

The decrease in RHWF by more than 75 % is one influential factor of the decrease in the ratio of RWHF to

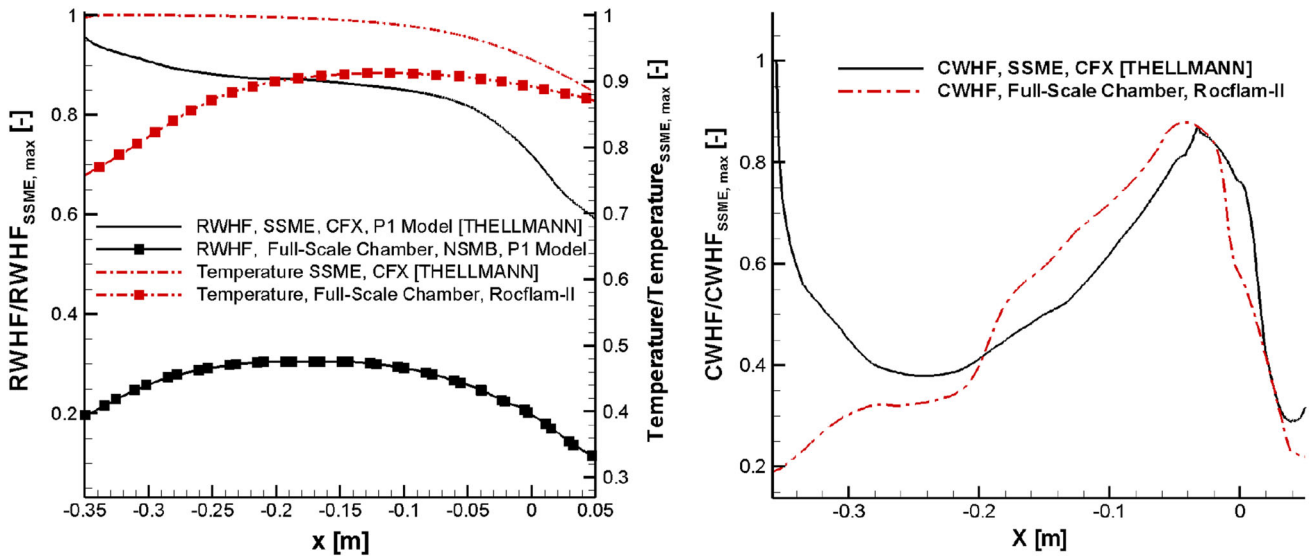

Fig. 19 Normalized RWHF (left) for Denison's WSGGM (homogeneous) and CWHF (right) over axial distance for the SSME [10] and a very high artificial load point of the fullscale combustion chamber of this work based on H_2/O_2 combustion

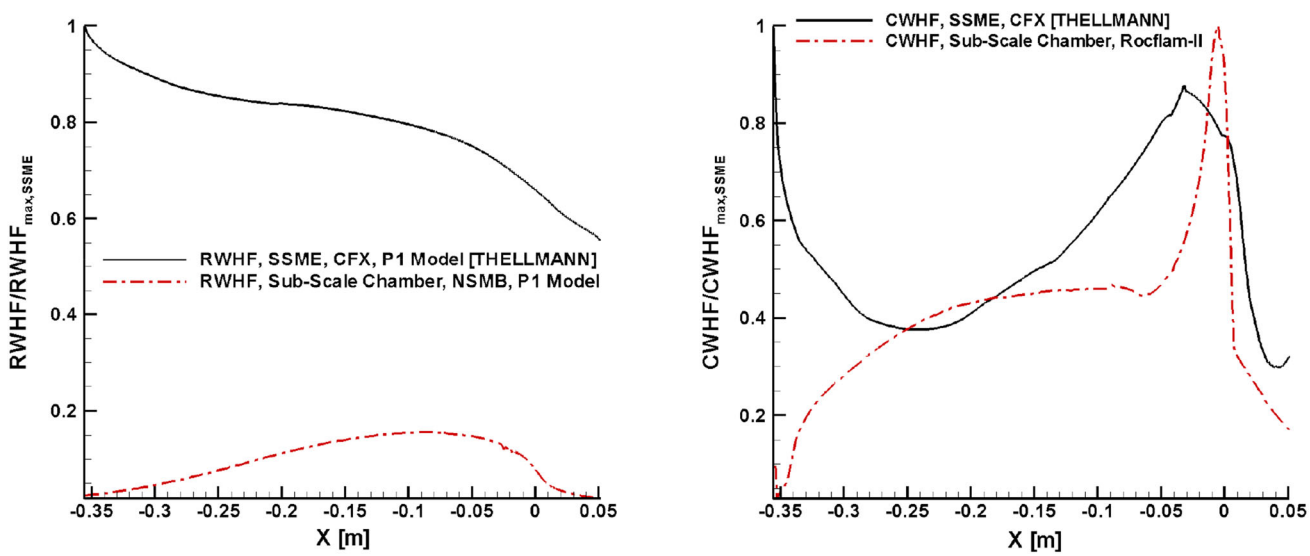

Fig. 20 Normalized RWHF (left) for Denison's WSGGM (homogeneous) and CWHF (right) over axial distance for the SSME [10] and the subscale combustion chamber of this work based on CH_4/O_2 combustion

TWHF for H_2/O_2 combustion. Besides that, the CWHF is different. Figure 19 shows the normalized CWHF for the fullscale combustion chamber of this work and for the SSME.

Except for a small part near the injector face plate, the predicted normalized CWHF of the SSME simulation is on the same level as for the fullscale combustion chamber in this work as intended by the artificially high load point. Only at the inlet the difference is quite strong as the propellant mixing effects are not taken into account in the SSME investigation. Consequently, assuming that the CWHF is roughly on the same level for most of the axial distances, the RWHF finally is the most influential source for the decrease of the ratio RWHF to TWHF.

For the SSME investigation the integrated ratio of RWHF to TWHF is 7.7 % compared to 3.3 % for the fullscale chamber in this work when using H_2/O_2 as propellants, which is a decrease of nearly 60 %. This decrease is caused by the RWHF which drops by 75 % from the SSME investigation to the fullscale combustion chamber in this work. Since the CWHF is slightly higher in the SSME investigation than in the fullscale chamber the decrease in the ratio RWHF to TWHF is in total reduced to only 60 %.

For CH_4/O_2 combustion only the results of the subscale chamber from this work can be compared to the results of the SSME powered by this fictitious propellant combination [10]. The integrated ratio of RWHF to TWHF for CH_4/O_2 combustion for the SSME is 8.8 % compared to around 1.9 % in the subscale combustion chamber of this work.

Looking at Fig. 20 one sees that the RWHF in the CH_4/O_2 combustion of this work is at maximum 20 % of the maximum RWHF in the SSME. At the inlet, this difference is even bigger than it has been for the H_2/O_2 combustion. Besides the temperature, due to the pre-burnt mixture entering the domain the sum of mass fractions for H_2O and CO_2 is a lot higher in the SSME case where it reaches nearly 99 % even at the inlet [10]. In contrast, the sum of mass fractions for H_2O and CO_2 in the subscale combustion chamber of this work is 5 % at the inlet and 70 % at its maximum downstream of the throat. It is obvious that with the increased amount of radiatively participating species plus the higher temperature, the RWHF is that much different in the SSME investigation.

In contrast to the H_2/O_2 propellant combination, the RWHF is not the only source of strong influence on the ratio of RWHF to TWHF. If it was, the difference in the ratio of RWHF to TWHF would be much bigger than it actually is. As Fig. 20 shows, the CWHF is also significantly higher over most parts of the axial distance in the SSME than in the current work predicted by Rocflam-II for the subscale chamber. Consequently, in the SSME investigation the ratio of RWHF to TWHF is only 8.8 % because the high RWHF is balanced by the high CWHF.

7 Summary and conclusion

Simulations of radiative heat transfer are carried out for H_2/O_2 combustion in subscale and fullscale combustion chambers and for CH_4/O_2 combustion in a subscale combustion chamber. Temperature, pressure and mole fractions of the radiating species H_2O and CO_2 are imported from Astrium's in-house CFD code Rocflam-II into the CFD code NSMB that has been utilized to solve radiative heat transfer. NSMB then determines parameters for the WSGG models and uses them to solve the P1 radiation transport model and finally yields the RWHF to the combustion chamber wall which is added to the CWHF given by Rocflam-II to yield the TWHF.

Simulations of the H_2/O_2 combustion confirm that the RWHF strongly depends on the temperature, reaching a maximum shortly upstream of the location of the maximum cross-sectionally averaged temperature. The influence of wall emissivity becomes obvious as the RWHF decreases linearly with decreasing emissivity of the combustion chamber wall. The maximum RWHF is comparable for both subscale and fullscale combustion chambers reaching around 1.7–1.8 % of their maximum CWHF for $\varepsilon = 0.6$, which represents a high but still realistic value for the wall emissivity. The different homogeneous WSGG models for the H_2/O_2 combustion have little influence on the RWHF for the subscale chamber whereas for the fullscale chamber the difference between Smith's and Denison's WSGGM increases which is caused by the less precise modeling of Smith's WSGGM. Using WSGGM capable of dealing with nonhomogeneous systems, the RWHF decreases to around 75 % of the homogeneous value for both combustion chambers in the H_2/O_2 combustion.

The local ratio of RWHF to TWHF has a maximum of around 10 % shortly downstream of the injector when using the homogeneous WSGGM. With the nonhomogeneous WSGGM the maximum ratio decreases to 5 % in the subscale chamber and to 3 % in the fullscale chamber.

The integrated ratio of RWHF to TWHF is around 3 % for $\varepsilon = 0.6$. The integrated ratio decreases linearly when the emissivity of the wall is reduced.

Coupling of radiation to the flow reveals no significant influence for the fullscale combustion chamber running on H_2/O_2. Neither the CWHF nor the temperature distribution in the flow field change perceptibly.

The dimension of the combustion chamber has an influence on the RWHF when Denison's WSGGM is applied as the RWHF increases in the fullscale chamber even though the load point and thus the maximum temperature in the fullscale chamber are comparable to the subscale chamber.

Simulations of the CH_4/O_2 subscale combustion chamber reveal a similar qualitative behavior of the RWHF over the axial distance, showing similar characteristics based on the cross-sectionally averaged temperature profile. In that combustion only H_2O and CO_2 are assumed to be radiatively participating. The influence of CO is not considered and the order of magnitude of the error introduced by that is shown to be similar to the influence of CO_2.

The simple homogeneous WSGG models by Smith, Copalle and Johansson yield nearly the same RWHF as the sophisticated model by Denison based on double integration and 121 gray gases. The simplified versions of Denison's homogeneous model predict only half of the other models' RWHF. The reason for that lies in the limitations of these options. With Denison's model for nonhomogeneous systems, the RWHF decreases by nearly 50 % of that predicted by the homogeneous models. For decreasing wall emissivities, the decrease of the RWHF is linear, too.

The local ratio of RWHF to TWHF for the CH_4/O_2 combustion behaves similar to the H_2/O_2 combustion having a slightly reduced maximum of 8 % near the injector faceplate based on homogeneous WSGGM. With the nonhomogeneous WSGGM by Denison, the maximum local ratio is less than 3 % at the injector faceplate.

The integrated ratio of RWHF to TWHF decreases compared to the H_2/O_2 combustion yielding a maximum of only 2.5 % for $\varepsilon = 0.6$ for the homogeneous WSGGM and 1.3 % for the nonhomogeneous WSGGM.

The findings of this work contradict the results of some of the former investigations of the SSME predicting a higher integrated ratio of RWHF to TWHF for both H_2/O_2 and CH_4/O_2 combustion. For both propellant combinations, the assumption of a pre-burnt mixture is found to be responsible for that. This yields too high estimates of temperature and species mass fractions which in turn lead to higher RWHF.

In conclusion one can say that it is essential for the prediction of a realistic RWHF to have a realistic flow field including temperature and species distribution. Concerning radiative transport the P1 model gives satisfactory results. More important appears the spectral modeling: Denison's detailed model for homogeneous systems shows comparable results to simpler models (i.e., Smith) for small optical path lengths as they appear in the subscale combustion chamber. At bigger path lengths, like in the fullscale chamber, the simpler models show a more pronounced deviation even though the general behavior as well as the order of magnitude is still acceptable. Using the nonhomogeneous WSGGM by Denison significantly decreases the RWHF compared to the homogeneous systems. Based on the homogeneous systems one can therefore acquire only rough estimates of maximum RWHF whilst for a precise prediction the nonhomogeneous models should be used.

Generally, one has to say that the contribution of gas radiation to the integral heat load of the chamber is relatively small even when assuming an elevated wall emissivity. Consequently, the use of simpler homogeneous models (i.e., Smith) implying a renouncement of accuracy appears to be acceptable when interested in a conservative estimate especially because all models predict the same qualitative evolution of RWHF. If one is interested in accurate quantitative predictions, the nonhomogeneous model by Denison fulfills this task best since it models the occurrence of hot lines and the corresponding increase in absorption more precisely and thus decreases the RWHF compared to the homogeneous models.

Acknowledgments The authors gratefully acknowledge support by Martin Göhring and Matthias Thoma who did most of the radiative transfer simulations as part of their Master's theses.

References

1. Smith, T.F., Shen, Z.F., Friedman, J.N.: Evaluation of coefficients for the weighted sum of gray gases model. ASME J. Heat Transf. **104**, 602–608 (1982)
2. Coppalle, A.: The total emissivities of high temperature flames. Combust. Flame **49**, 101–108 (1983)
3. Denison, M.K., Webb, B.W.: An absorption-line blackbody distribution function for efficient calculation of total gas radiative transfer. J. Quant. Spectrosc. Radiat. Transf. **50**, 499–510 (1993)
4. Johansson, R.: Account for ratios of H_2O to CO_2 in the calculation of thermal radiation of gases with the weighted-sum-of-grey-gases model. In: Proceedings of the Sixth Mediterranean Combustion Symposium (2009)
5. Denison, M.K., Webb, B.W.: The spectral line-based weighted-sum-of-gray-gases model in nonisothermal nonhomogeneous media. J. Heat Transf., ASME **117**(2), 359–365 (1995)
6. Vos, J.B., Rizzi, A.W., Corjon, A., Chaput, E., Soinne, E.: Recent advances in aerodynamics inside the NSMB (Navier Stokes multi block) consortium, Aerospace Sciences Meeting and Exhibit, 36th, Reno (1998)
7. Göbel, F., Mundt, Ch.: Implementation of the P1 radiation model in the CFD solver NSMB and investigation of radiative heat transfer in the SSME main combustion chamber, 17th AIAA International Space Planes and Hypersonic Systems and Technologies Conference (2011)
8. Naraghi, M.H., Dunn, S., Coats, D.: Modeling of Radiation Heat Transfer in Liquid Rocket Engines, AIAA-2005-3935, Joint Propulsion Conference, Arizona (2005)
9. Wang, T.-S.: Unified Navier–Stokes flowfield and performance analysis of liquid rocket engines. J. Propuls. Power **9**(5), 678–685 (1993)
10. Thellmann, A.: Impact of Gas Radiation on Viscous Flows, in Particular on Wall Heat Loads, in Hydrogen–Oxygen vs. Methane–Oxygen Systems, Based on the SSME Main Combustion Chamber. Universität der Bundeswehr München, Ph.D. thesis, Institute of Thermodynamics (2010)
11. Göbel, F., Birgel, D., Thellmann, A.: CFD Simulation of Hydrogen–Oxygen and Methane–Oxygen System for Space Shuttle Main Combustion Chamber including Radiative Effects. 60th International Astronautical Congress (2009)
12. Göbel, F., Mundt, Ch.: CFD Analysis of Radiative Heat Transfer in the SSME Main Combustion Chamber using Advanced Spectral Models, 7th European Symposium on Aerothermodynamics for Space Vehicles (2011)
13. Frey, M., Aichner, Th., Görgen, J., Ivancic, B., Kniesner, B., Knab, O.: Modeling of Rocket Combustion Devices, 10th AIAA/ASME Joint Thermophysics and Heat Transfer Conference, Chicago, IL (2010)
14. Siegel, R., Howell, J.R.: Thermal Radiation Heat Transfer. McGraw-Hill, Tokyo (1972)
15. Capra, B.R.: Aerothermodynamic Simulation of Subscale Models of the FIRE II and Titan Explorer vehicles in Expansion Tubes, Ph.D. thesis, University of Queensland (2007)
16. Modest, M.F.: Radiative Heat Transfer, 2nd edn. Academic Press, San Diego, London, Burlington (2003)
17. Göbel, F.: Implementation of Spectral Models for Gas Radiation into the CFD Solver NSMB and Validation on the basis of the SSME Main Combustion Chamber. Deutscher Luft- und Raumfahrtkongress, DLRK 2010-1357, Hamburg (2010)
18. Denison, M.K., Webb, B.W.: An absorption line blackbody distribution function for efficient calculation of total gas radiative transfer. J. Quant. Spectrosc. Radiat. Transf. **50**(5), 499–510 (1993)
19. Denison, M.K., Webb, B.W.: The spectral-line weighted-sum-of-gray-gases model for H_2O/CO_2 mixtures. J. Heat Transf. **117**(3), 788–792 (1995)
20. Görgen, J., Aichner, Th, Frey, M.: Spray Combustion and Heat Transfer Modelling in LOX/H2, LOX/HC and MMH/NTO Combustion chambers, 3rd edn. European conference for Aerospace Sciences (EUCASS), Versailles (2009)
21. McBride, B.J., Gordon, S.: Computer Program for Calculating and Fitting Thermodynamic Functions, NASA RP-1271 (1992)
22. GASPAK, Software Package, Cryodata Inc. http://www.htess.com/gaspak.htm [cited January, 6th 2014]

23. Göhring, M.: Numerische Simulation der ungekoppelten Gasstrahlung in modernen H_2/O_2 Raketenbrennkammern, Master's thesis, Institute of Thermodynamics, Universität der Bundeswehr München (2011)
24. Touloukian, Y.S.: Thermophysical Properties of Matter, vol. 7. Thermal Radiative Properties, Metallic Elements and Alloys, New York (1970)
25. Kniesner, B., Frey, M., Knab, O.: Numerical Investigation of Gas Generator and Preburner Flows for Rocket Engine Applications, 4th European Conference for Aerospace Sciences (EUCASS). St. Petersburg, Russia (2011)